Materialia 7 (2019) 100401

Contents lists available at ScienceDirect

Materialia

journal homepage: www.elsevier.com/locate/mtla

Full Length Article

Effect of aluminum titanate on the fracture mechanism of the nickel–zirconia system under uniaxial and biaxial strength testing conditions

Madisen W. McCleary [a], Roberta Amendola [a,*], Stephen J. Walsh [b], Benjamin P. McHugh [a]

[a] Mechanical and Industrial Engineering Department, Montana State University, 220 Roberts Hall, Bozeman, MT 59717, United States
[b] Department of Mathematical Sciences, Montana State University, 2-214 Wilson Hall, Bozeman, MT 59717, United States

ARTICLE INFO

Keywords:
Ceramic
Mechanical properties
Fracture mechanisms
SOFC
Scanning electron microscopy
Weibull statistics

ABSTRACT

Solid Oxide Fuel Cell (SOFC) anodes were fabricated with NiO–YSZ and 0–10 wt% aluminum titanate (Al_2TiO_5, ALT) addition. Samples were manufactured using a tape casting procedure to a thickness of approximately 500 μm. A remarkable enhancement of the mechanical strength, up to 166%, was found when compared to the samples without ALT addition. The development of secondary phases was observed proportional to the amount of aluminum titanate. Mechanical properties evaluation was conducted using uniaxial and biaxial strength testing. Weibull statistics was used for mechanical properties analysis and an advanced statistical analysis was employed to identify the existence of multiple flaw populations. Fractography was performed on selected samples to elucidate the fracture mechanisms. Biaxial testing was characterized by high mechanical strength with lower Weibull moduli; whereas, uniaxial testing showed lower mechanical strength and higher Weibull moduli. It was found that the addition of 0%, 5% and 10% ALT to Ni–YSZ samples exhibit a fracture mechanism that is dependent on one flaw population namely porosity and mechanical strength of secondary phases, respectively. Samples without the addition of ALT were characterized by intergranular fracture while transgranular fracture was found for the addition of 5% and 10% ALT to Ni–YSZ samples. For the addition of 1% ALT to Ni–YSZ samples both flaw populations were identified. Analysis of the fracture surfaces revealed the simultaneous presence of intergranular and transgranular features. It is proposed that secondary phases, developed by ALT addition, increase the mechanical strength of the material shifting the fracture mechanism from intergranular to transgranular.

1. Introduction

A solid oxide fuel cell (SOFC) is an energy conversion device which electrochemically oxidizes a fuel to produce electrical power and heat. SOFCs are a promising renewable energy system; therefore, over the past several decades, research efforts have focused on improving their performance and longevity. Recently, there has been growing interest in anode supported SOFCs because of the improved single cell (cathode, electrolyte, anode assembly) performance [1–7]. To achieve the desired power output, single cells are then stacked in electrical series where contact is achieved through high clamping pressures e.g., 65–70 kPa [8,9]. In these systems, the anode layer is the thickest and provides the mechanical strength of the stack. Once assembled and during operation, the SOFC stack is exposed to additional stresses resulting from thermal expansion mismatch between the components and temperature gradients which, may further compromise the mechanical stability leading to premature failure of the system. Ni–YSZ composites are widely used as anode material due to their low cost, good electronic conductivity, chemical stability, catalytic properties and compatibility with other materials in SOFCs. However, in contrast to the vast amount of data available on the electrochemical properties of Ni–YSZ composites, little fundamental data on the mechanical performance exists and minimal data is available on the mechanism responsible for the failure of the material.

The mechanical performance of ceramics depends on random microstructural flaw distribution; specifically, the weakest spot under stress determines the material strength [10]. Uniaxial flexural tests, such as three- or four-point bending, have long been used to determine ceramic material strength. During these testing, a rectangular sample is submitted to uniaxial load. The maximum stress goes from tensile to compressive throughout the sample thickness and is experienced at the surface. This measurement technique however, may only provide a partial characterization of the material load bearing capacity due to the sample's geometry that introduces low curvature radius defects (sample edges) acting like stress concentrators [11]. Also, advanced engineering ceramic components often fail due to multiaxial stress conditions. For these reasons, several multiaxial strength tests have been developed.

* Corresponding author.
E-mail address: roberta.amendola@montana.edu (R. Amendola).

https://doi.org/10.1016/j.mtla.2019.100401
Received 10 April 2019; Accepted 7 July 2019
Available online 13 July 2019

Biaxial flexural tests on disc-shaped specimens like ring-on-ring or ball-on-ring are particularly favored because the maximum tensile stress occurs at the center of the surface opposite to load application; consequently, edge flaws do not influence the results [12–19].

The inherently brittle nature of the anode causes big scatter in fracture strength measurement. Large batches of material must be tested and Weibull statistical analyzes must be used basing on the assumption that the weakest spot under tension determines the strength of the sample. The "size effect" relative to tensile strength is quite prominent in ceramics. As the size of a test specimen is increased, then, on an average, the tensile strength of the component decreases giving the wrong impression of a weaker material. The reason is that as the sample volume is increased, the likelihood of encountering a critical flaw with deleterious orientations to the load applied increases [20–24].

Correlation of results obtained by different testing methodologies is possible when the same volume of material under tension is considered. This variable is known as the "effective volume" [25]. The effective volume is a function of the sample geometry and corresponds to the size of a hypothetical tension test specimen that, when stressed to the same level as the sample in question, has the same probability of failure. It is implied that the same type of volume distributed flaws control strength in each geometry. Through effective volume, Weibull parameters and measured characteristic strength, the strength values obtained with different testing methodologies and sample geometries can be scaled and properly compared.

Previous research has shown that the formation of secondary phases, due to the addition of small amounts of foreign oxides (e.g., CeO_2, Nb_2O_5, Al_2O_3) to the NiO–YSZ system during the manufacturing process, has resulted in improved electrochemical performance [6,7,26,27,28]. ALT doping of the Ni/YSZ system has yielded to the formation of secondary phases which contributed to dramatically improved catalyst thermal resilience as well as processing conditions which offer maximum efficacy [29–31]. Due to the need for the anode to provide the mechanical support to the stack once assembled, the authors conducted studies on effect of ALT addition on the mechanical properties of the Ni-YSZ-ALT system to complement the enhanced electrochemical properties. Results showed that the formation of secondary phases also results in enhanced strength of the material [32]. This work however is to be considered only preliminary. Test have been conducted on bulk samples (~2 mm thick) with a thickness and a final porosity after processing that are not appropriate for actual use in anode supported systems. Currently, little fundamental data on the mechanical performance of the proposed, or similar material exist and almost no literature is available on the mechanism responsible for its failure. Due to the promising enhanced electrochemical and mechanical behavior of the Ni–YSZ–ALT system, this study performs further characterization to fill this knowledge gap and towards the optimization of the material.

Ni–YSZ SOFC anodes under uniaxial and biaxial strength testing conditions is evaluated. The validity of both testing methods is discussed based on the experimental evidence. Tape casting is used to manufacture samples with the thickness appropriate for anode supported systems (~0.5 mm). Advanced statistical analysis (finite mixture distribution modeling) is used to characterize non-linear pattern in the Weibull-linear plot to identify multiple flaw populations. Fractography is then used to relate flaw populations to specific secondary phases microstructural features. It has been proposed that secondary phases, developed by ALT doping addition, increase the mechanical strength of the material shifting the fracture mechanism from intergranular to transgranular.

2. Experimental

Powders of nickel oxide (NiO) (4 μm, Alfa Aesar), 8 mol% yttria-stabilized zirconia (YSZ) (300 nm, Tosoh) and aluminum titanate (ALT) (25 nm, Sigma Aldrich) were used for manufacturing of the anode material. Powders, in the ratio of 34 wt% YSZ, 66 wt% NiO and 0–10 wt% ALT, were mechanically mixed for 24 h with binder and deionized water. Solids loading for the slurry was 48 wt%. Plasticizers and binders used were polyvinyl alcohol (4 wt%), xanthan gum (<1 wt%), Rhoplex (24 wt%), polyethylene glycol (2 wt%), Dynol 604 (<1 wt%), and Duramax D-3005 (1 wt%), Surfynol PC Defoamer (<1 wt%). The NiO to YSZ ratio (66:34) was held constant when ALT was added; the overall percentages were adjusted accordingly (e.g. for 5 wt% ALT addition, the powder ratios would be 62.7 wt% for NiO, 32.3 wt% for YSZ and 5 wt% for ALT). Tape casting was used for sample manufacturing. The slurry was taped with a doctor blade gap of 2 mm and dried in ambient conditions. Subsequently, 6 × 40 mm rectangular samples for uniaxial strength testing (three-point bending, TPB) were cut with a rotary blade and 32 mm circular samples were punched out for biaxial strength testing (ring on ring, ROR).

Binder thermolysis was performed in a Thermolyne 1300 furnace as follows: (1) heating to 150 °C at 2 °C/min, (2) 2 h dwell, (3) heating to 450 °C at 0.5 °C/min, (4) heating to 1100 °C at 5 °C/min (5) 2 h dwell for partial sintering, and (6) cooling to room temperature at 10 °C/min Partial sintering was performed to allow for safe sample handling while transferring to the Zircar, Hot Spot 110 for subsequent sintering. Sintering was conducted with a heating/cooling rate of 5 °C/min up to 1500 °C and a 2 h dwell time. Final sintered size for the rectangular samples was 5 × 0.5 × 25 mm and ø25 × 0.5 mm for the circular ones.

Reduction was performed in a Thermo Scientific, Lindberg Blue M tube furnace flowing 5% H_2–95% N_2 gas, at 800 °C for a time sufficient time to convert 97 wt% of NiO into metallic nickel. The percentage reduction was evaluated with a Radwag XA 82/220.R2 microscale. In the presented manufacturing conditions, ALT spontaneously decomposes to Al_2O_3 and TiO_2 [28]. The Al_2O_3 initially reacts with NiO to form $NiAl_2O_4$ [23,29,31,33,34] as follows:

$$NiO + Al_2O_3 \rightarrow NiAl_2O_4 \quad (1)$$

Basing on reaction (1), the system is depleted of an amount of NiO proportional to the Al_2O_3 introduced with ALT addition. The amount of NiO available for reduction has therefore been evaluated accounting for $NiAl_2O_4$ formation.

Ni–YSZ anode samples with the addition of 0, 1, 5 and 10 wt% ALT in batches of 30 reduced samples were loaded at a rate of 0.2 mm/min in a TPB apparatus (Pasco Scientific 8236) and in a ROR apparatus (Instron 5543) as per ASTM C1161-13 and ASTM C1499 – 15 standards, respectively [14,35]. The test fixture for the TPB apparatus had a support span of 16 mm and the ROR apparatus had a bottom and top support ring diameter of 20 mm and 7 mm, respectively. For both testing methods, recorded strength corresponded to the maximum values obtained under monotonic application of the load which refers to a test conducted at the selected constant rate in a continuous fashion, with no reversals from test initiation to final fracture. Fracture strength, effective volume (V_{eff}), scaled characteristic strength (σ_0'), Weibull modulus (m) with normalized upper and lower bounds, and porosity, by alcohol immersion method, were evaluated for the testing conditions. Field emission scanning electron microscopy (FE-SEM, Zeiss Ultra) was conducted to determine the nature of the developed phases and their contribution to the mechanical strength and to elucidate the material failure mechanism.

3. Results and discussion

3.1. Mechanical properties

The maximum likelihood Weibull approach which considers that the weakest flaw under tension determines the strength of the material has been used. Weibull plots are created by formulating the two-parameter Weibull equation (Eq. (2)) into a straight line form (Eq. (3)) where the slope is the Weibull modulus [36].

$$p_s = \exp\left(-\frac{\sigma}{\sigma_0}\right)^m \quad (2)$$

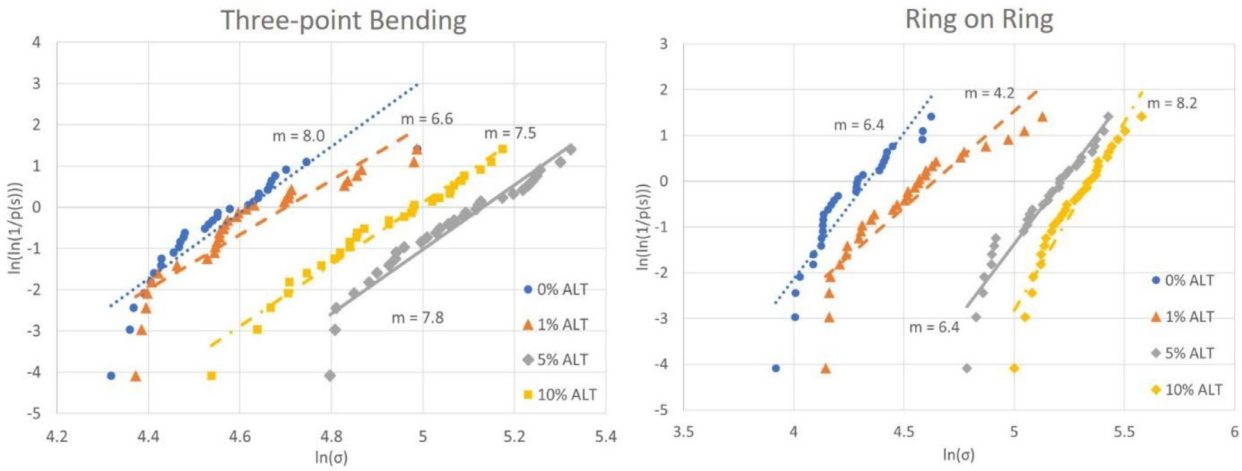

Fig. 1. Weibull plots of uniaxial (TPB) and biaxial (ROR) strength testing.

Table 1
Mechanical properties and porosity of uniaxial (TPB) and biaxial (ROR) strength testing samples.

	0 wt% ALT	1 wt% ALT	5 wt% ALT	10 wt% ALT
TPB				
Porosity (%)	45.5	42.5	29.7	23.0
Weibull Modulus	8.0	6.6	7.8	7.5
90% Confidence Interval	6.0–9.8	4.9–8.0	5.8–9.5	5.6–9.1
Characteristic Strength (MPa)	102	115	170	147
V_{eff} (mm^3)	0.28	0.32	0.27	0.35
Scaled Characteristic Strength (MPa)	82	87	142	127
Strength Increase (%)	N/A	6	73	54
ROR				
Porosity (%)	45.9	42.0	29.1	23.1
Weibull Modulus	6.4	4.2	6.4	8.2
90% Confidence Interval	4.8–7.8	3.2–5.1	4.8–7.8	6.2–10.0
Characteristic Strength (MPa)	77	94	184	210
V_{eff} (mm^3)	2.23	3.75	2.43	1.67
Scaled Characteristic Strength (MPa)	82	128	212	220
Strength Increase (%)	N/A	55	157	166

$$\ln\left(\ln\left(1/p_s\right)\right) = m\ln(\sigma/\sigma_0) \tag{3}$$

Where p_s is the probability of survival for each sample, m is the Weibull modulus, σ is the flexural strength (MPa) of each sample, and σ_0 is the characteristic strength (MPa) calculated at a probability of failure of $1/e$. Fig. 1 shows the Weibull plots, along with the corresponding Weibull moduli.

Since the probability to encounter a flaw depends on the tested volume, the effective volume (V_{eff}) was calculated and averaged for each batch of 30 samples. As the TPB and ROR samples have different geometries, two different equations (Eqs. (4) and (5)) were used for the calculation as follows [25]:

$$V_{effTPB} = \frac{lwh}{2(m+1)^2} \tag{4}$$

$$V_{effROR} = \left\{\frac{\pi}{2}D_L^2\right\}\left\{1+\left[\frac{44(1+\upsilon)}{3(1+m)}\right]\left[\frac{5+m}{2+m}\right]\left(\frac{D_S-D_L}{D_S D}\right)^2 \times\left[\frac{2D^2(1+\upsilon)+\left(D_S-D_L\right)^2(1-\upsilon)}{(3+\upsilon)(1+3\upsilon)}\right]\right\}\left\{\frac{h}{2(m+1)}\right\} \tag{5}$$

Where l is the span between bottom support points in mm, w is the width of the sample in mm, h is the height of the sample in mm, m is the Weibull modulus, D_L is the diameter of the loading ring in mm, D_S is the diameter of the support ring in mm, D is the diameter of the sample in mm, υ is the Poisson's ratio (assumed to be 0.3) [20].

Considering the effective volume, the characteristic strength for each batch can be scaled for comparison. Eq. (6) has been used to calculate the scaled characteristic strength [23].

$$\sigma_0' = \sigma_0\left(\frac{V_{eff}}{1\ mm^3}\right)^{\frac{1}{m}} \tag{6}$$

Where σ_0' is the scaled characteristic strength in MPa, σ_0 is the characteristic strength in MPa, V_{eff} is the effective volume in mm^3, and m is the Weibull modulus.

The 90% confidence interval of the Weibull modulus was determined per ASTM C1239-13 for each batch of 30 samples [37–39]. Table 1 summarizes the mechanical properties and the porosity of the anode material with the addition of ALT tested in the TPB and the ROR fixtures.

An increased characteristic strength for samples with ALT addition, when compared to the ones without ALT, is found for both the testing methodologies. This confirms the benefit of ALT addition that was previously observed for bulk material (2 mm thick) of the same composition [32]; showing that, such benefit, transfers to a smaller thickness (500 μm) which is more appropriate to be considered for an anode supported fuel cell architecture.

The same manufacturing process was used for all the tested batches and well relates to the consistency of the porosity values. During the sintering process, the decomposition of ALT leads to the formation of $NiAl_2O_4$ proportional to the amount of ALT. This reaction depletes the system of NiO available for reduction resulting in a lower porosity when

compared to the 0% ALT samples [34]. The strength of ceramics is dependent on the porosity distribution within the material [22,23,40–42] since the presence of one or more pores in the loaded volume will result in a more fragile material.

It was previously found [43] that ceramics with porosity between 10 and 55%, which well represents the materials of this study, resulted in Weibull modulus values in the range between 4 and 11 with a medium to high scatter in the fracture strength regardless of the composition, grain size, testing techniques or surface finish of the specimens. The failure of these kind of materials has been linked to the pore evolution during the sintering process. A few anomalies, however, point out the fact that porosity may not be the only mechanism responsible for the failure of the material and needs further investigation.

Studies comparing uniaxial and biaxial strength testing in ceramics [11,44–46], show higher strength values for biaxial than uniaxial testing, in accordance with this study. Processing flaws, which mostly concentrate upon the surface of specimens, facilitate crack initiation and fracture. Comparing with TPB specimens, ROR specimens were not influenced by the presence of edge flaws; therefore, ROR testing recorded higher characteristic strength values when compared to TPB and may better represent the material intrinsic behavior.

The effect of the V_{eff} is another factor that should be considered in the material evaluation because the probability to apply stress to a flaw increases if the tested volume under tension is larger. Thus, the measured strength is larger if the tested volume is smaller, giving a wrong impression of a stronger material.

For the TBP samples, the 0% and 5% ALT material show very similar Weibull moduli and V_{eff}; specifically, 8 and 0.28 mm^3 for the 0% versus 7.8 and 0.27 mm^3 for the 5% ALT samples. The recorded scaled characteristic strength values are 82 and 142 MPa, respectively. Basing on the very similar V_{eff}, the 73% strength increase may be related to the decrease in porosity from 45.5% to 29.7% and seems to support what was stated earlier. Despite the beneficial effect on the material strength, it must be considered that the appropriate amount of porosity (minimum ~30%) must be assured for its successful electrochemical performance. For the 10% ALT samples, the Weibull modulus and effective volume are 7.5 and 0.35 mm^3, porosity decreases to 23% while the scaled characteristic strength decreases to 127 MPa. When considering the 10% ALT samples, it is expected that the ~7% additional decrease in porosity from the 5% ALT value, would nullify the effect of the 0.8 mm^3 increase in the V_{eff}; instead, a 19% decrease of the scaled characteristic strength is observed when compared to the 5% ALT samples. This shows that porosity is not the only variable responsible for the failure of the material. This comparison shows that the Weibull modulus is not enough to provide information on the material reliability since values were all very close but other variables must be accounted for. It is hypothesized that a concurrent mechanism contributing to the material failure is related to the mechanical strength of secondary phases developed with the addition of ALT and will be discussed later.

For the ROR samples, a proportionality between ALT amount and characteristic strength is observed. The 1% ALT samples show that indeed, a decrease in porosity prevails over an increased V_{eff} resulting in higher characteristic strength when compared to the 0% ALT samples.

For both TPB and ROR testing, the lowest Weibull modulus was calculated for the 1% ALT samples. When compared to the 0% ALT material, the decreased porosity (from ~45% to ~42%), should result in lower data scattering which should be reflected in an increased Weibull modulus. Instead the opposite behavior is observed while an increased scaled characteristic strength is recorded. The lower Weibull modulus confirms the possibility of a porosity concurrent failure mechanism that relates to the change in the material microstructure due to the effect of secondary phase development.

Advanced statistical analyses along with fractography of select samples will be discussed in the next sections to further elucidate the material failure mechanisms.

3.2. Advanced statistical analysis to identify presences of multiple fractographic populations

ASTM C1239-13 provides detailed methodology for characterizing data when multiple flaw populations are present, often expressed as a non-linear pattern in the Weibull-linear plot. When multiple flaw populations are evident the standard approaches to parameter estimation (e.g., Weibull modulus and characteristic strength) are not applicable [47] because multiple flaw distributions may not be well-characterized by a single set of Weibull parameters, and if so a more detailed analysis is required.

Two different flaw populations are suspected for the material in this study: a first one related to porosity and a second one related to the mechanical strength of secondary phases developed during the addition of ALT. An advanced statistical modeling technique, finite mixture distribution modeling, was implemented is as follows to measure the strength of evidence provided by each specimen data set in support of multiple populations:

1. Identify presence of multiple populations: assess each batch of strength data for evidence of multiple fractographic populations via finite mixture modeling. If the data provides evidence for more than one population, each individual specimen will then be classified into a sub-population distribution.
2. For each identified population: select representative samples across the strength distribution for fractographic analysis to characterize the fracture mechanism. To accurately represent the entire strength distribution, samples were selected based on the 5-number summary of the strength distribution: minimum, 25%tile, median, 75%tile, maximum.

3.3. Finite mixture modeling and assessing evidence for multiple strength distributions

A sample batch containing a single strength distribution may be characterized by a single Weibull distribution via estimating the parameters of the following probability density function (Eq. (7)):

$$f(x;\ \theta = (m,\ \beta)) = \left(\frac{m}{\beta}\right)\left(\frac{x}{\beta}\right)^{m-1} \exp\left[-\left(\frac{x}{\beta}\right)^{m}\right] \tag{7}$$

where x represents the strength measurement of a single specimen, m is the Weibull modulus and β is the characteristic strength.

If the strengths are generated by $K < \infty$ distinct flaw distributions (fractographic populations), then the probability density function for this situation (Eq. (8)) may be written as:

$$g(x;\ \theta_1,\ \ldots, \theta_K) = \sum_{i=1}^{K} \pi_i * f(x;\ \theta_i) \tag{8}$$

where θ_i is a distinct set of Weibull parameters for the ith component of the mixture distribution and π_i represents the probability weighting of each mixture component where $\sum_{i=1}^{K} \pi_i = 1$. The model has several unknown parameters for a given data set: K (number of distributions in the mixture), each set of Weibull parameters θ_i, and the mixture probabilities π_i. Advanced statistical methods, specifically the Expectation-Maximization algorithm, were developed to determine the best parameters for a specific set of data [47]. The 'mixR' package from the *R* statistical programming language, which has validated applications of these algorithms [48,49], was used. The procedure was implemented as follows:

1. Assess the best number of mixture components K for a specific specimen set: up to $K = 3$ distributions were searched in each strength data set. Evidence for the best number of mixture components is provided by the *Bayesian Information Criteria (BIC)* [48,50]. The model with the smallest BIC is selected as best representation of the data.

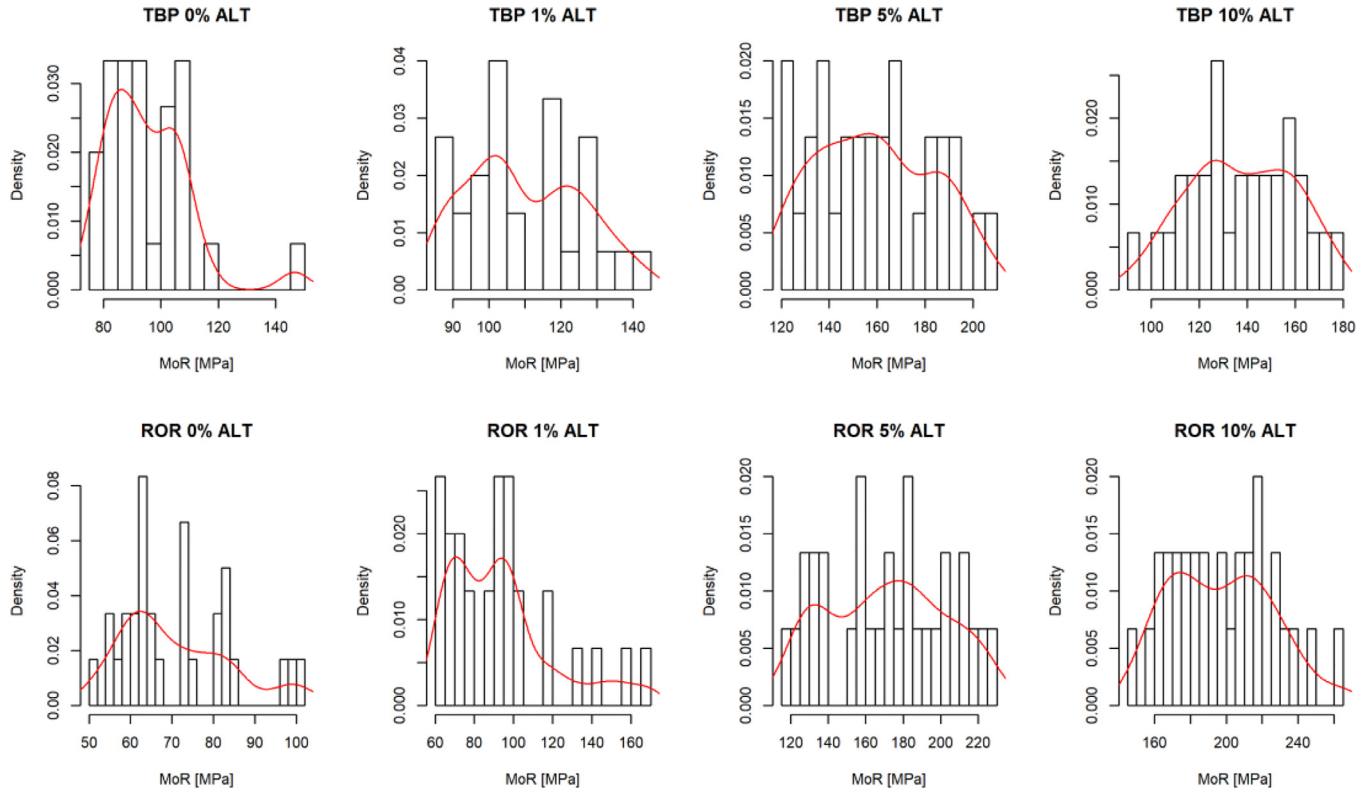

Fig. 2. Histograms and Probability Density Estimates for the TPB and ROR sample data, 0–10% ALT.

Table 2
BIC values for model selection.

	Number of Populations			Minimum ΔBIC
	1	2	3	
	Model BIC			
TPB				
0 wt% ALT	0.0000	N/A	N/A	N/A
1 wt% ALT	0.0000	2.9327	10.9575	2.9327
5 wt% ALT	0.0000	6.1595	13.4104	6.1595
10 wt% ALT	0.0000	7.2083	16.0234	7.2083
ROR				
0 wt% ALT	1.7373	0.0000	1.7282	1.7282
1 wt% ALT	0.0773	0.0000	9.1568	0.0773
5 wt% ALT	0.0000	7.6213	6.8657	6.8657
10 wt% ALT	0.0000	5.9976	13.9862	5.9976

2. Classify: based on the selected model, each specimen is classified into a specific distribution via estimation of *responsibilities* [51]. Responsibilities are estimates of posterior probabilities *for each specimen* that communicate how likely the specimen is to belong to a specific component of the mixture.

As a first assessment, distribution summaries are presented in graphical form in Fig. 2. The plots show the probability density of the strength data for each specimen with an overlying curve estimating its distribution. Multiple modes in the density curve present some evidence for existence of multiple distributions. If 2 populations are identified as proposed in Section 3.1, the expected pattern is bi-modal (presenting two peaks). As this assessment is only qualitative, further tools must be implemented to confirm the presence of multiple populations in the data.

To quantify the evidence for multiple populations mixture distributions are fit with $K = 1, 2, 3$ components. BIC is used to select the best model. Table 2 summarizes the data which are minimum BIC subtracted with $\Delta BIC_K = BIC_K - \min(BIC)$. Therefore, the best model corresponds to a $\Delta\text{BIC} = 0$. It is common to use $\Delta BIC_K < 2$ as a measure of equal evidence in support of competing models while $2 < \Delta BIC_K < 6$ as positive but not conclusive evidence in support of a model.

For both TPB and ROR 5% and 10% ALT sample batches, 1 population was confirmed. $K = 1$ mixture components presented the strongest evidence with $\Delta BIC_K = 0$ and the next largest $\Delta BIC_K > 6$. For the TPB 0% sample batch, only the $K = 1$ model can be applied.

For the ROR test, the $K = 2$ mixture component model was strongly supported for 0% and 1% ALT batches. For the TPB test, the 1% ALT batch, the $K = 2$ model is positively but not conclusively supported ($\Delta BIC_2 = 2.9327$). For these batches, the $K = 2$ mixture component model was applied, then model responsibilities were estimated. Model responsibilities are defined as the probability that each individual specimen belongs to each distribution. The result of this analysis is shown in Fig. 3. The left panel shows the full probability density and each fitted mixture density on the histogram. The right panel shows, for each specimen, the responsibility. Data have been classified into distribution 1 or 2 by selecting a threshold of 0.5.

With each data characterized to distribution 1 or 2, fractographic characterization by FE-SEM was performed on selected representatives from each strength distribution (minimum, 25%tile, median, 75%tile, maximum) to elucidate the failure mechanism.

3.4. Microstructural analyses

Investigation of samples' surfaces by FE-SEM was performed to asses secondary phases development. Since the same manufacturing process was used for all batches, the same morphology was found on both TPB and ROR samples and is presented in Fig. 4. The developed phases are consistent with previous author's findings [32]. The "rough phase" (circled in Fig. 4(c)), forms during the sintering process, persists unaltered after reduction and it enlarges proportionally to the amount of ALT. TiO_2 from ALT decomposition, preferentially reacts with YSZ enhancing its sintering characteristics [7,29,31] and leading to the formation of

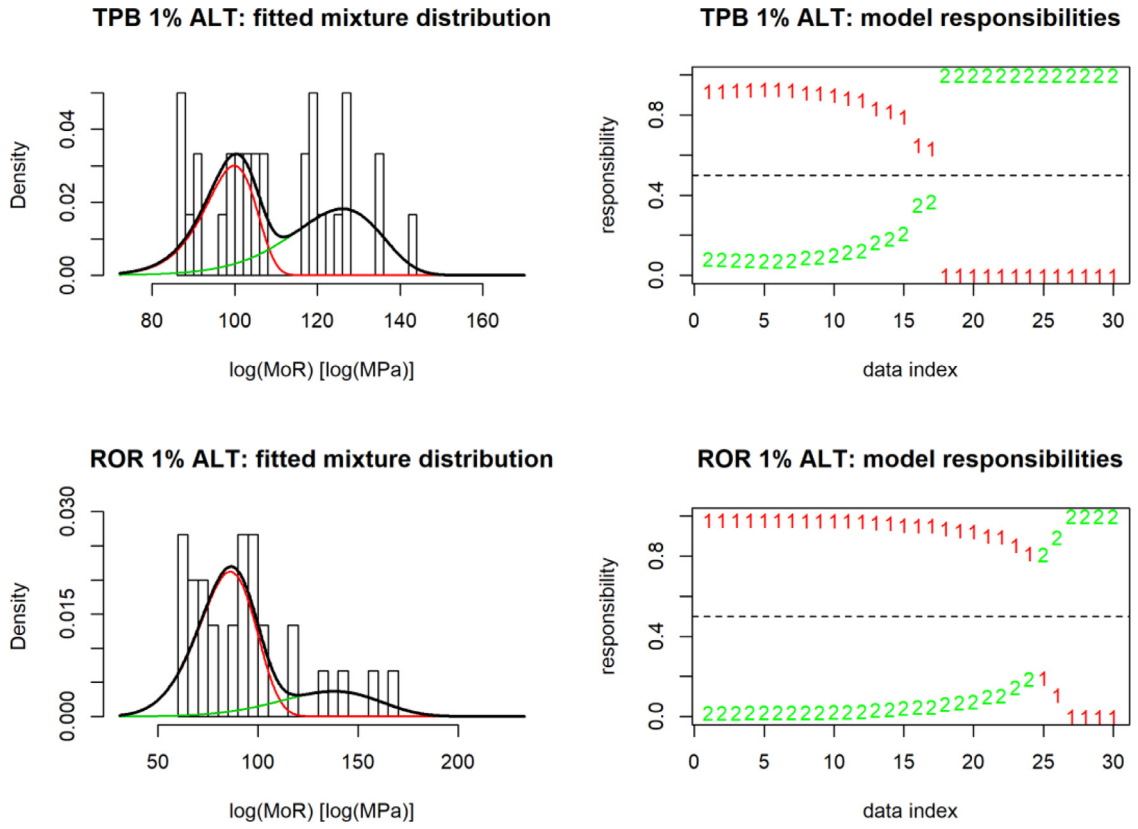

Fig. 3. Probability density with fitted Weibull Mixture distribution (left) and model responsibilities for each specimen (right).

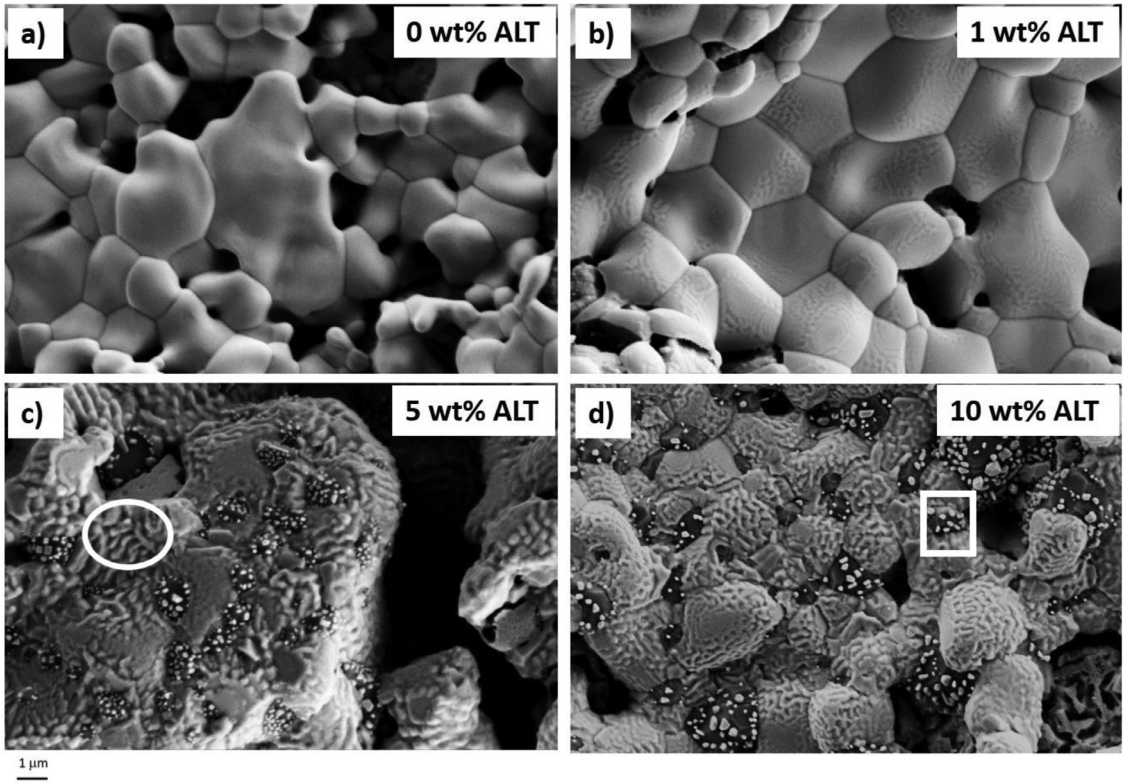

Fig. 4. FE-SEM surface morphology of uniaxial (TPB) and biaxial (ROR) strength testing samples with (a) 0 wt% ALT, (b) 1 wt% ALT, (c) 5 wt% ALT and (d) 10 wt% ALT.

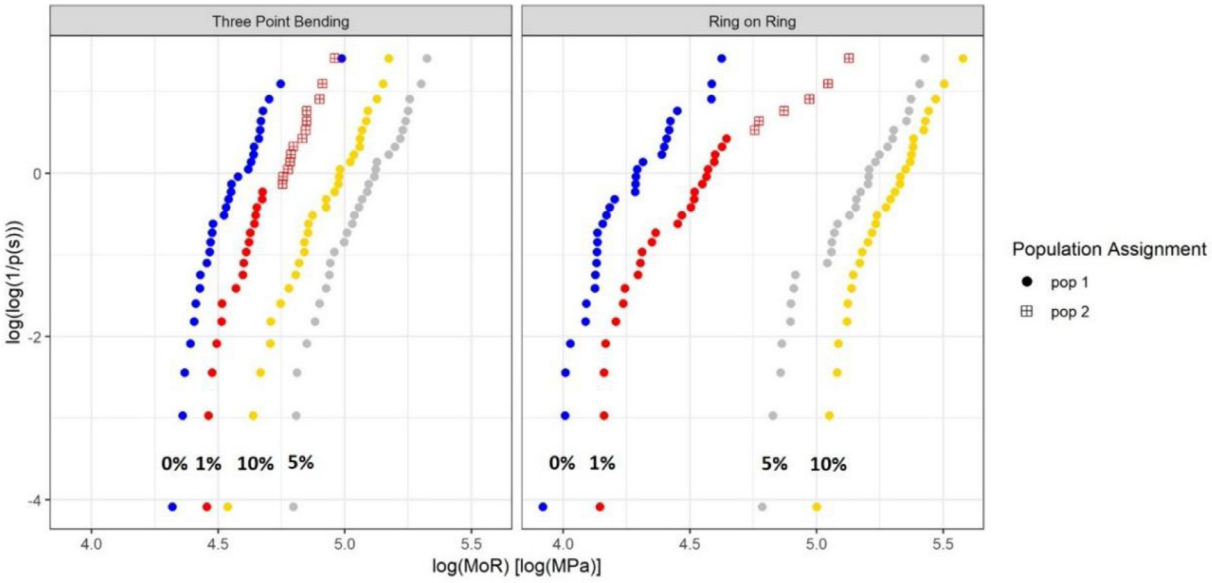

Fig. 5. Weibull plots with populations denoted for uniaxial (TPB) and biaxial (ROR) strength testing.

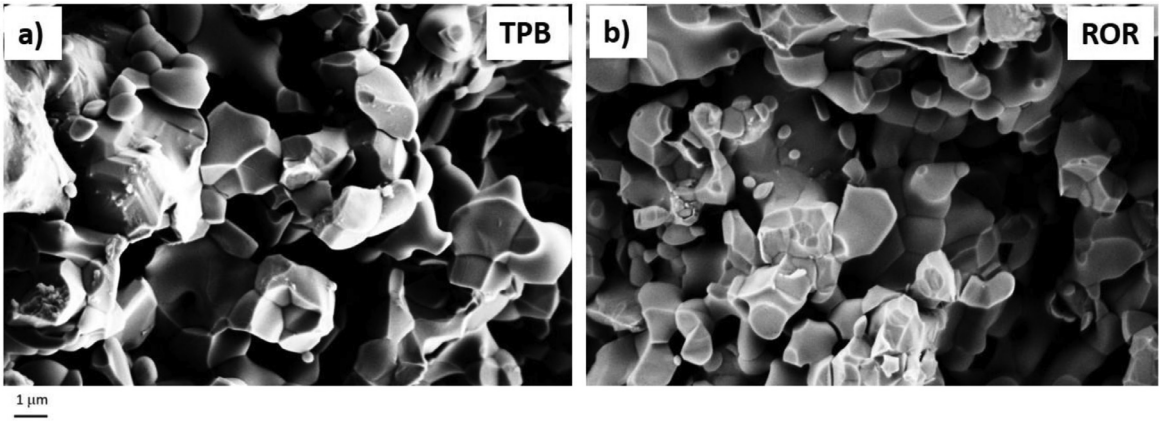

Fig. 6. Fracture surface of 0% ALT sample batches with (a) TPB and (b) ROR testing methods.

a solid YSZ framework. The contribution to the enhanced material mechanical strength is to be related to the volume change resulting from a tetragonal to monoclinic stress induced phase transformation caused by the thermal expansion mismatch with the other material components while in the oxidized state namely NiO, YSZ, Al_2O_3, and $NiAl_2O_4$ [7,32]. The "small particle phase" (boxed in Fig. 4(d)) is due to the partial reduction of $NiAl_2O_4$ leading to the formation of Ni nanoparticles within an Al_2O_3 matrix [32,34,52]. The contribution to the enhanced material strength is due to the nickel acting either as crack deflector or stopping the crack propagation due to its ductility [23,32,52,54].

Despite the non-linear pattern in the Weibull plot of the 0% ALT samples, evidence showed that there is only one flaw population to be considered. The same "cluttered" pattern, with several data points lying on the same line, was found for both testing methodologies. It is thought that porosity is the volume flaw responsible for the material failure not depending on the testing method [43]. Fig. 6 is representative of the fracture surface of the 0% ALT sample batches. Selected samples, as described earlier, were analyzed and the fracture surface morphology was found to be similar for all of them showing a clear intergranular (along the grain) fracture pattern. The data points "cluttering" phenomenon is hypothesized to be related to flaws generating cracks that require a similar amount of energy to propagate.

The 5% and 10% ALT batches also showed evidence of single flaw population. Very similar fracture surface morphologies were found for the representative samples and are shown in Fig. 7.

For all samples a clean and flat surface corresponding to transgranular (through the grain) failure can be observed. The lower values of the scaled characteristic strength recorded for the TPB when compared to the ROR are related to the "edge effect" but the mechanisms responsible for the failure of the material is proposed to be the same. In the "small particle" phase, tensile stresses are generated within the Ni particles due to the coefficient of thermal expansion mismatch experienced during the sintering and reduction processes [32,52,53]. This places the surrounding Al_2O_3 phase in a state of compressive stress, increasing its strength. It is hypothesized that the interface between the nickel particles and Al_2O_3 is the volume flaw responsible for the material failure. The mechanical strength of such interface varies within the material depending on the aforementioned stress distribution. Fig. 4 shows how, within the material, regions of the "small particle" phase are distributed within region of the "rough phase" (YSZ framework). It is hypothesized that, in the "small particle" phase, a crack grows under an increasing applied load until it reaches a critical size where the remaining uncracked section of the material (YSZ framework) can no longer support the applied stress at which point complete fracture occurs. Fig. 7 supports this

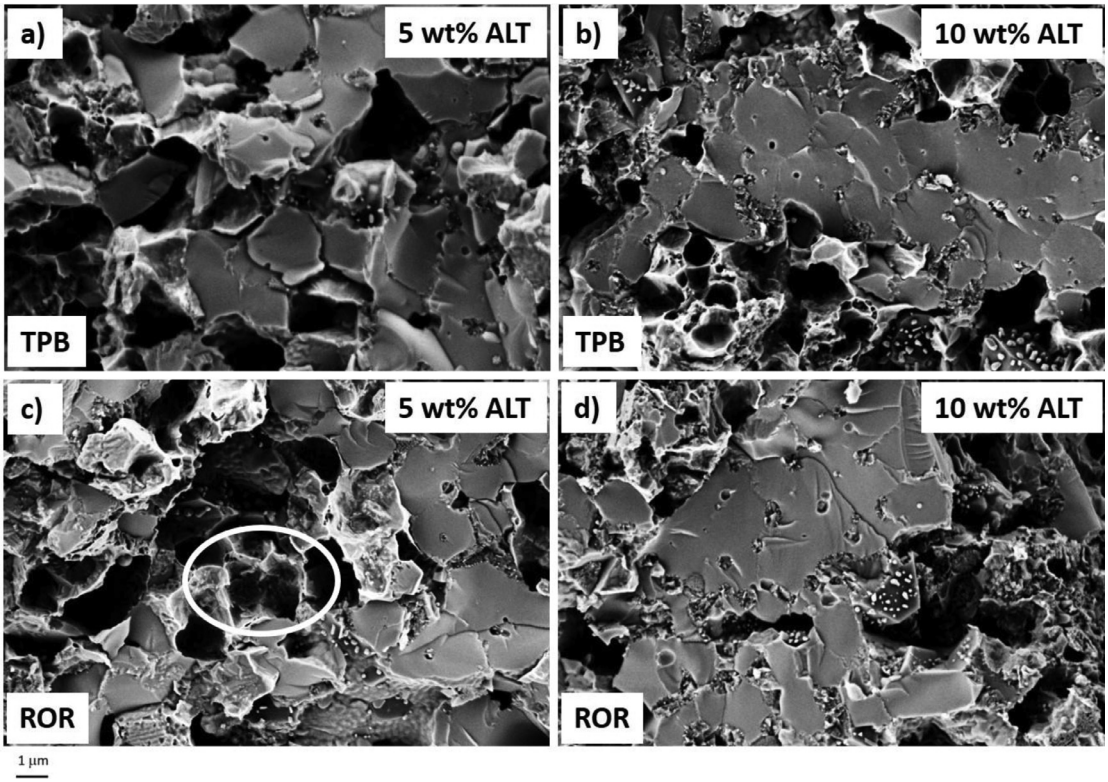

Fig. 7. Fracture surfaces of (a) and (c) 5% and (b) and (d) 10% ALT sample batches fractured with (a) and (b) TPB and (c) and (d) ROR testing methods.

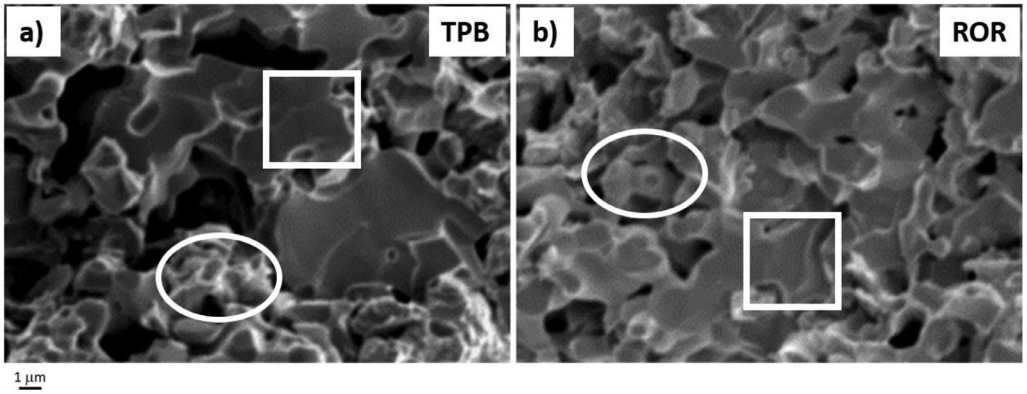

Fig. 8. Fracture surface morphology of 1% ALT Ni-YSZ after (a) TPB and (b) ROR testing.

hypothesis showing that a small amount of plastic deformation (circled ductile lips in Fig. 7(c)) occurred before fracture. It is believed that this is due to the nickel adding ductility to the system. During crack propagation, stresses will be transferred from the Al_2O_3 substrate to the metallic phase which will yield, deform and then ultimately fail allowing for the crack to reach the undamaged material.

The 1% ALT samples showed evidence of the two identified flaw populations. Fractographic analyses confirmed the presence of both intergranular and transgranular features, circled and boxed in Fig. 8, respectively. When compared to the 0% ALT samples, the strength increase recorded with TPB and ROR testing are 6% and 55% (Table 1). It must be noted that, the scaled characteristic strength increases due to the formation of $NiAl_2O_4$ and the Ti-YSZ framework [32]. The onset of the $NiAl_2O_4$ reduction process requires ~10 h [33]. The 97% reduction at this amount of ALT, is reached after ~4 h; therefore, the small particle phase does not form. Population 2 (mechanical strength of secondary phases) is defined as the one including data points falling in the upper tail of the strength distribution (Fig. 5). For TPB testing, thirteen data points out of the thirty belong to population 2, while for biaxial strength testing it is six. This research has highlighted that ROR strength testing better depicts the overall material mechanical performance. The low ALT amount (1%) results in a smaller volume covered by the secondary phases; therefore, the overall beneficial effect is expected to be limited. This well agrees with a smaller number of data points belonging to population 2.

In these cases, where one population distribution occurs in a small number of test specimens, it is not necessary to re-estimate Weibull parameters. Estimates of the Weibull parameters for this flaw distribution would be potentially biased with wide confidence bounds [47].

4. Conclusions

This study has demonstrated that ALT addition can enhance the mechanical properties of Ni–YSZ systems through secondary phases devel-

opment. Uniaxial and biaxial strength testing have been used to evaluate mechanical properties. An enhancement of the characteristic strength up to 166% has been observed for 10% ALT addition with biaxial strength testing. It has been found that biaxial strength testing better depicts the overall material mechanical performance. The use of different testing methodologies along with advanced statistical analyses has allowed for the identification of two flaw populations that are responsible for the material failure namely, porosity and mechanical strength of secondary phases. Fractography performed on selected samples has allowed for elucidation of the failure mechanism. A single flaw population has been identified for 0% ALT samples. Intergranular fracture has been observed and the failure has been linked to porosity. Samples with ALT addition ≥ 5% are also characterized by a single flaw population. Transgranular fracture has been observed and the failure has been linked to the mechanical strength of the secondary phases; specifically, the strength of the interface between nickel nanoparticles and their alumina substrate. The presence of both flaw populations was found for the low ALT level (1%). Fracture surfaces have been characterized by the presence of both intergranular and transgranular features. It has been proposed that secondary phases, developed by ALT addition, increase the mechanical strength of the material shifting the fracture mechanism from intergranular to transgranular. Despite the benefits offered by the presence of the "small particles phase", it has been reported in literature that in accelerated testing condition at higher temperature and in reduction medium Ni particles agglomerates due to sintering. This phenomenon can compromise the long-term performance of fuel cell. The authors understand that, for the materials to be optimized, more testing in fuel cell operative conditions is needed.

Declaration of interests

None.

Acknowledgments

This work was supported by the DOE under award number DE-FE0031125. The statistical analyses were supported by the NSF under award number DMS-1748883. FE-SEM analyses were conducted at the Montana State University Image and Chemical Analysis Laboratory.

References

[1] F. Zhao, A.V. Virkar, Dependence of polarization in anode-supported solid oxide fuel cells on various cell parameters, J. Power Sources 141 (2005) 79–95, doi:10.1016/j.jpowsour.2004.08.057.
[2] A.C. Müller, D. Herbstritt, E. Ivers-Tiffée, Development of a multilayer anode for solid oxide fuel cells, Solid State Ionics 152–153 (2002) 537–542, doi:10.1016/S0167-2738(02)00357-0.
[3] Z.R. Wang, J.Q. Qian, S.R. Wang, J.D. Cao, T.L. Wen, Improvement of anode-supported solid oxide fuel cells, Solid State Ionics 179 (2008) 1593–1596, doi:10.1016/j.ssi.2008.03.022.
[4] T. Setoguchi, K. Okamoto, K. Eguchi, H. Arai, Effects of anode material and fuel on anodic reaction of solid oxide fuel cells, J. Electrochem. Soc. 139 (1992) 2875–2880, doi:10.1149/1.2068998.
[5] M. Kleitz, F. Petitbon, Optimized SOFC electrode microstructure, Solid State Ionics 92 (1996) 65–74, doi:10.1016/S0167-2738(96)00464-X.
[6] C.R. He, W.G. Wang, Alumina doped Ni/YSZ anode materials for solid oxide fuel cells, Fuel Cells 9 (2009) 630–635, doi:10.1002/fuce.200800152.
[7] M. Mori, Y. Hiei, H. Itoh, G.A. Tompsett, N.M. Sammes, Evaluation of Ni and Ti-doped Y_2O_3 stabilized ZrO_2 cermet as an anode in high-temperature solid oxide fuel cells, Solid State Ionics 160 (2003) 1–14, doi:10.1016/S0167-2738(03)00144-9.
[8] T. Dey, D. Singdeo, M. Bose, R.N. Basu, P.C. Ghosh, Study of contact resistance at the electrode-interconnect interfaces in planar type solid oxide fuel cells, J. Power Sources 233 (2013) 290–298, doi:10.1016/j.jpowsour.2013.01.111.
[9] T. Dey, A. Dey, P.C. Ghosh, M. Bose, A.K. Mukhopadhyay, R.N. Basu, Influence of microstructure on nano-mechanical properties of single planar solid oxide fuel cell in pre- and post-reduced conditions, Mater. Des. (2014), doi:10.1016/j.matdes.2013.06.052.
[10] J.R. Lund, J.P. Byrne, Leonardo da Vinci's tensile strength tests: implications for the discovery of engineering mechanics, Civ. Eng. Environ. Syst. 18 (2001) 243–250, doi:10.1080/02630250108970302.
[11] Y. Xu, J. Han, H. Lin, L. An, Comparative study of flexural strength test methods on CAD/CAM Y-TZP dental ceramics, Regen. Biomater. 2 (2015) 239–244, doi:10.1093/rb/rbv020.
[12] D. Munz, T. Fett, Ceramics: Mechanical Properties, Failure Behaviour, Materials Selection, 2001, doi:10.1070/sm1981v038n03abeh001340.
[13] R. Morrell, N.J. McCormick, J. Bevan, M. Lodeiro, J. Margetson, Biaxial disc flexure – modulus and strength testing, Br. Ceram. Trans. 98 (1999) 234–240, doi:10.1179/096797899680507.
[14] Standard Test Method For Monotonic Equibiaxial Flexural Strength of Advanced Ceramics At Ambient Temperature, ASTM Int., 2015, pp. 1–19, doi:10.1017/CBO9781107415324.004.
[15] D.K. Shetty, A.R. Rosenfield, P. McGuire, G.K. Bansal, W.H. Duckworth, Biaxial flexure tests for ceramics, Am. Ceram. Soc. 12 (1980) 1193–1197.
[16] M.N. Giovan, G. Sines, Biaxial and uniaxial data for statistical comparisons of a ceramic's strength, J. Am. Ceram. Soc. 62 (1979) 510–515, doi:10.1111/j.1151-2916.1979.tb19117.x.
[17] B.J. Hulm, J.D. Parker, W.J. Evans, Biaxial strength of advanced materials, J. Mater. Sci. 33 (1998) 3255–3266, doi:10.1023/A:1013216825960.
[18] M.I. Abu-Hassan, O.A. Abu-Hammad, A. Harrison, Strains and tensile stress distribution in loaded disc-shaped ceramic specimens. An FEA study, J. Oral Rehabil. 25 (1998) 490–495, doi:10.1046/j.1365-2842.1998.00267.x.
[19] G.A. Thompson, Determining the slow crack growth parameter and weibull two-parameter estimates of bilaminate disks by constant displacement-rate flexural testing, Dent. Mater. 20 (2004) 51–62, doi:10.1016/S0109-5641(03)00068-X.
[20] A. Nakajo, J. Kuebler, A. Faes, U.F. Vogt, H.J. Schindler, L.K. Chiang, S. Modena, J. Van Herle, T. Hocker, Compilation of mechanical properties for the structural analysis of solid oxide fuel cell stacks. Constitutive materials of anode-supported cells, Ceram. Int. 38 (2012) 3907–3927, doi:10.1016/j.ceramint.2012.01.043.
[21] H. Fischer, W. Rentzsch, R. Marx, A modified size effect model for brittle nonmetallic materials, Eng. Fract. Mech. 69 (2002) 781–791, doi:10.1016/S0013-7944(01)00126-6.
[22] H.L. Frandsen, T. Ramos, A. Faes, M. Pihlatie, K. Brodersen, Optimization of the strength of SOFC anode supports, J. Eur. Ceram. Soc. (2012), doi:10.1016/j.jeurceramsoc.2011.11.015.
[23] B. Charlas, D.W. Ni, H.L. Frandsen, K. Brodersen, M. Chen, Mechanical properties of supports and half-cells for solid oxide electrolysis influenced by alumina–zirconia composites, Fuel Cells 17 (2017) 132–143, doi:10.1002/fuce.201600036.
[24] F. Baratta, W. Matthews, Errors associated with flexure testing of brittle materials, U.S. Army Mater. Technol. Lab. 16 (1987) 41–42.
[25] Standard Practice for Size Scaling of Tensile Strengths using Weibull Statistics for Advanced Ceramics, ASTM Int., 2015, pp. 1–18, doi:10.1520/C1683.
[26] D.R. Driscoll, B.W. Tokmakian, N.P. Johnson, C.D. Hunt, S.W. Sofie, Catalyst enhancing aluminum titanate for increasing strength of nickel–zirconia cermets, Mater. Lett. 209 (2017) 307–310, doi:10.1016/j.matlet.2017.08.035.
[27] S.W. Sofie, D.R. Taylor, Controlled thermal expansion anode compositions with improved strength for use in anode supported SOFCs, Adv. Solid Oxide Fuel Cells III (2008) 215–223.
[28] P.K. Tiwari1, S. Basu, CeO_2 and Nb_2O_5 modified Ni-YSZ anode for solid oxide fuel cell, Ionics (Kiel) 23 (2017) 2571–2577, doi:10.1007/s11581-016-1945-1.
[29] D.R. Driscoll, M.D. McIntyre, M.M. Welander, S.W. Sofie, R.A. Walker, Enhancement of high temperature metallic catalysts: aluminum titanate in the nickel-zirconia system, Appl. Catal. A Gen. 527 (2016) 36–44, doi:10.1016/j.apcata.2016.08.020.
[30] D. Driscoll, C. Hunt, J. Muretta, S.W. Sofie, Thermally stabilized nickel electrocatalyst introduced by infiltration for high temperature electrochemical energy conversion, ECS Trans. 53 (2013) 63–72, doi:10.1149/05309.0063ecst.
[31] C.H. Law, S.W. Sofie, Anchoring of infiltrated nickel electro-catalyst by addition of aluminum titanate, J. Electrochem. Soc. 158 (2011) B1137–B1141, doi:10.1149/1.3610226.
[32] M. Mccleary, R. Amendola, Effect of aluminum titanate (Al_2TiO_5) doping on the mechanical performance of solid oxide fuel cell Ni-YSZ anode, Fuel Cells (2017) 862–868, doi:10.1002/fuce.201700073.
[33] J. Zygmuntowicz, P. Wiecinska, A. Miazga, K. Konopka, Characterization of composites containing $NiAl_2O_4$ spinel phase from Al_2O_3/NiO and Al_2O_3/Ni systems, J. Therm. Anal. Calorim. 125 (2016) 1079–1086, doi:10.1007/s10973-016-5357-2.
[34] M. McCleary, R. Amendola, Reduction kinetics of undoped and aluminum titanate (Al_2TiO_5) doped NiO-YSZ solid oxide fuel cell anodes, Ceram. Int. 44 (2018) 15557–15564, doi:10.1016/j.ceramint.2018.05.218.
[35] Standard Test Method For Flexural Strength of Advanced Ceramics At Ambient Temperature, ASTM Int., 2013, pp. 1–19, doi:10.1520/C1161-13.2.
[36] J.B. Quinn, G.D. Quinn, A practical and systematic review of Weibull statistics for reporting strengths of dental materials, Dent. Mater. 26 (2010) 135–147, doi:10.1016/j.dental.2009.09.006.
[37] Z. Cui, Y. Huang, H. Liu, Predicting the mechanical properties of brittle porous materials with various porosity and pore sizes, J. Mech. Behav. Biomed. Mater. 71 (2017) 10–22, doi:10.1016/j.jmbbm.2017.02.014.
[38] D. Wu, Y. Li, J. Zhang, L. Chang, D. Wu, Z. Fang, Y. Shi, Effects of the number of testing specimens and the estimation methods on the Weibull parameters of solid catalysts, Chem. Eng. Sci. 56 (2001) 7035–7044, doi:10.1016/S0009-2509(01)00340-2.
[39] A. Khalili, K. Kromp, Statistical properties of Weibull estimators, J. Mater. Sci. 26 (1991) 6741–6752.
[40] M. Radovic, E. Lara-curzio, Elastic properties of nickel-based anodes for solid oxide fuel cells as a function of the fraction of reduced NiO, J. Am. Ceram. Soc. 87 (2004) 2242–2247, doi:10.1111/j.1151-2916.2004.tb07499.x.
[41] M. Radovic, E. Lara-Curzio, Mechanical properties of tape cast nickel-based anode materials for solid oxide fuel cells before and after reduction in hydrogen, Acta Mater. 52 (2004) 5747–5756, doi:10.1016/j.actamat.2004.08.023.
[42] Z. Cui, Y. Huang, H. Liu, Predicting the mechanical properties of brittle porous materials with various porosity and pore sizes, J. Mech. Behav. Biomed. Mater. 71 (2017) 10–22, doi:10.1016/j.jmbbm.2017.02.014.

[43] X. Fan, E.D. Case, F. Ren, Y. Shu, M.J. Baumann, Part I: porosity dependence of the Weibull modulus for hydroxyapatite and other brittle materials, J. Mech. Behav. Biomed. Mater. 8 (2012) 21–36, doi:10.1016/j.jmbbm.2011.12.010.
[44] J. Jin, H. Takahashi, N. Iwasaki, Effect of test method on flexural strength of recent dental ceramics, Dent. Mater. J. 23 (2004) 490–496, doi:10.4012/dmj.23.490.
[45] G.K.R. Pereira, M. Amaral, R. Simoneti, G.C. Rocha, P.F. Cesar, L.F. Valandro, Effect of grinding with diamond-disc and -bur on the mechanical behavior of a Y-TZP ceramic, J. Mech. Behav. Biomed. Mater. 37 (2014) 133–140, doi:10.1016/j.jmbbm.2014.05.010.
[46] K. Zeng, A. Odén, D. Rowcliffe, Flexure tests on dental ceramics, Int. J. Prosthodont. 9 (1996) 434–439. http://www.ncbi.nlm.nih.gov/pubmed/9108743.
[47] Standard Practice for Reporting Uniaxial Strength Data and Estimating Weibull Distribution Parameters For Advanced Ceramics, ASTM Int., 2013, pp. 1–9, doi:10.1520/C1239-13.Scope.
[48] D.D. Boos, L.A. Stefanski, Essential Statistical Inference: Theory and Methods, 2013 New York, doi:10.1016/j.peva.2007.06.006.
[49] R. Gentleman, R. Ihaka, R Computer Program, (2019). https://www.r-project.org/.
[50] Y. Youjiao, mixR: finite mixture modeling for raw and binned data, (2018). https://cran.r-project.org/package=mixR.
[51] C. Bishop, Pattern Recognition and Machine Learning, 2006 New York, doi:10.1021/jo01026a014.
[52] E. Üstündağ, R. Subramanian, R. Dieckmann, S.L. Sass, In-situ formation of metal-ceramic microstructures in the Ni–Al–O system by partial reduction reactions, Acta Mater. 43 (1995) 383–389, doi:10.1016/0167-2738(94)00148-L.
[53] E. Üstündag, Z. Zhang, M.L. Stocker, P. Rangaswamy, M.A.M. Bourke, J.A. Roberts, S. Subramanian, K.E. Sickafus, S.L. Sass, Influence of residual stresses on the evolution of microstructure during the partial reduction of $NiAl_2O_4$, Mater. Sci. Eng. A. 238 (1997) 50–65.
[54] M. Lieberthal, W.D. Kaplan, Processing and properties of Al_2O_s nanocomposites reinforced with sub-micron Ni and $NiAl_2O_4$, Mater. Sci. Eng. A. 302 (2001) 83–91, doi:10.1016/S0921-5093(00)01358-7.